ISSN 0915-633X

NATIONAL INSTITUTE FOR FUSION SCIENCE

Anomalous Heat Evolution of Deuteron Implanted Al on Electron Bombardment

K. Kamada, H. Kinoshita and H. Takahashi

(Received - May 9, 1995)

NIFS-361 June 1995

RESEARCH REPORT
NIFS Series

NAGOYA, JAPAN

Anomalous heat evolution of deuteron implanted Al on electron bombardment

K. Kamada, H. Kinoshita(1) and H. Takahashi(1)

National Institute for Fusion Science, Nagoya,

464-01 Japan.

(1)Department of Engineering, Hokkaido University,

Sapporo, 062 Japan

Abstract

Anomalous heat evolution, which is presumed to continue for about 2 $\times 10^{-11}$ seconds, was observed in deuteron implanted Al foils on 175 keV electron bombardment. Local regions with linear dimension of more than 100nm each showed simultaneous transformation from single crystalline to polycrystalline structure in roughly one minutes on the electron bombardment, indicating the temperature rise up to more than melting point of Al from room temperature. The amount of energy evolved was typically 160MeV for each transformed region. The transformation was never observed in proton implanted Al foils.

Microstructures in the subsurface layer of the implanted Al, investigated by the collaboration of ERD and TEM, were presented for numerical discussions of the experimental results.

Possible causes of the surface melting, such as heating effect of the electron beam, size effect of the melting point, difference of the implanted depth profiles between the hydrogen and deuterium, and possible chemical reactions due to the electron bombardment in D_2 collections were investigated, and the conclusion was inevitable that some kind of nuclear reactions which takes place in the D_2 collections is responsible for the melting.

(KEYWORDS; deuteron implantation, electron bombardment, melting)

1. Introduction

In a previous papers [1,2] , one of the authors (K.K.) reported an anomalous particle emission phenomenon from H_3^+ or D_3^+ implanted Al foil on 200 or 400keV electron bombardment. In the papers, the author

presumed that fusion reactions to take place not only between deuterons but also between protons, which were embedded in the so called "Tunnel Structure" (T.S.), created in a sub-surface layer of Al on the implantations. One of the prominent features of this phenomenon was that it is not due to the energetic collisions between reacting particles. This was derived in the paper [1] from the calculation on the fusion reaction rate between knocked-on deuterons, produced by the electron bombardment, and embedded deuterons. In the present state of our knowledge, however, we cannot present any conclusive mechanism of the phenomenon.

In the present paper, a direct observation of this anomalous phenomenon via heat evolution leading to very local melting of deuterium implanted Al on 175 keV electron bombardment is reported. The direct observation was made by the transmission electron microscope (TEM), which at the same time served as an electron accelerator.

2. Experiment

We first implanted Al specimens with 25 keV D_2^+ ions. The specimens were prepared beforehand so as to enable TEM observations after the implantation. They were polished chemically from Al disk with 5^{mm} diameter and 0.1^{mm} thick using TENUPOLE chemical polishing machine. The purity of the Al was 99.99%, and the specimens were annealed at 400℃ for 3 hours before the polishing. After the polishing they have wedge shape with average thickness of more than 1 μ m over an area of about 1mm diameter and have a small hole of about 0.1mm diameter in the central part

of each specimen.

The fluence of the implanted deuteron was chosen around 5×10^{17} D^+/cm^2, since below this amount of fluence only a bubble structure is formed in the sub-surface layer of Al foil, and above that so called "Tunnel Structure" (T.S.) is produced [3,4].

The implanted specimens were then examined by TEM at room temperature at about 20minutes, or on keeping them in liquid nitrogen for 24hours or more, after the implantation. The TEM used was Hitachi H-700, operated at 175 keV to avoid radiation damage of Al.

3. State of the implanted hydrogen isotopes in Al.

In previous papers [3,4], the state of the implanted hydrogens was observed by simultaneous employment of the two experimental methods, the Elastic Recoil Detection(ERD) using 2MeV helium beam and the TEM observations. These two methods were applied on the same Al specimen, first applying the ERD for depth profiling of the implanted hydrogen during and after the implantation. Then the TEM observation was done on the same specimen profiled to observe the microstructure of the implanted subsurface layer. As results of these investigations, we found following things about the implanted state of hydrogens.

Below $5 \times 10^{17} H_1^+/cm^2$ of hydrogen ion fluence, the implanted hydrogens form the molecular coagulations compressed into bubbles with estimated pressure of roughly 7GPa [4]. Further implantation over the above fluence produces the T.S. connecting so far produced bubbles at the depth of roughly 100nm, in the case of 25keV H_2^+ implantation, below a

surface. (The mechanism of the T.S. formation is not very clear at present, but, on the basis of these observation, we believe that the Al atoms are all evacuated from the region and there remains a long void filled with hydrogen molecules.) Right after the T.S. formation, the number of bubbles becomes very small, then increases again gradually on further implantation [4]. The tunnel structure occupies 50 to 100nm of depth as observed from stereoscopic TEM observations, and roughly 60 to 70% of a surface area when seen perpendicularly to the implanted surface. The maximum amount of the hydrogen atoms retained in the subsurface layer was estimated from the maximum retention, 1×10^{17} H atoms/cm^2 [3], and the FWHM, about 60 nm, of the hydrogen profile obtained by ERD, giving 2×10^{22} H atoms/cm^3. For deuterium, very close values to that of hydrogen was obtained by one of the authors [5]. After the implantation, some of the implanted hydrogen escapes out of the surface. By the depth profiling method, one of the authors (K,K) has measured the decrease of the hydrogen molecule $\triangle H_2$ up to 3 days and obtained the following empirical formulae

$$-\frac{\triangle H_2}{H_2^{\circ}} = 10^{-1.51}\cdot t^{0.218} \qquad (1)$$

at room temperature, where H_2° is the initial amount of hydrogen molecule and t is in seconds.

Table 1 tabulates the change of density of the hydrogen/deuterium molecules in T.S. calculated by eq.(1), taking the initial value

$H^{\circ}_{2} = D^{\circ}_{2} = 1 \times 10^{22} cm^{-3}$, together with the molar volume, i.e. the inverse of the density, and the corresponding pressures. The pressures were obtained from the equation of states (EOS) of pressurized hydrogen and deuterium measured by Michels et al. [6] at 25℃. These values of the pressures were confirmed with more recent EOS's obtained by Mills et al. [7,8]. So, we conclude that thermodynamical state of the deuterium in the T.S. is a fluid state.

In this treatment we assumed that all the implanted hydrogen atoms coagulate into the tunnel structure as molecules. This would be approvable by the fact that hydrogen solubility is extremely low in Al matrix, that is about 5×10^{-6} at room temperature.

In the case of hydrogen isotope implantation, we should be aware of the fact that deuteron has smaller energy loss in Al than that of proton of the same energy below about 200keV [9]. Therefore, the range of the deuteron is longer than proton in the present experiment. However, implanted hydrogens,and deuterons as well, never reside around the range in Al, but they flow back toward the implanted surface, and stay around the depth of the energy loss peak, that is around the depth of the maximum of the lattice defect production. This is clearly shown in Fig.1, where (a) and (b) are the ERD profiles of implanted hydrogen and deuteron, respectively. Both profiles almost coincide with the respective energy loss maxima, which are calculated with TRIM computer code (not shown for brevity). Further, we like to emphasize, for later discussions, that the depths to reside on the implantation are almost the same for both hydrogen and deuterium within the experimental error of ERD.

4. Experimental results

Two micrographs of Fig.2 show the typical examples of TEM observations taken on the Al specimens implanted with hydrogen, (a), and with deuteron, (b), respectively. Regions of brighter contrast in both micrographs are the T.S. regions, where Al atoms are evacuated and, instead, hydrogen or deuterium molecules are contained. In the micrograph (b), we can observe several areas, like the one indicated by an arrow, where something looks like microcrystallites are concentrated. These speckled areas appear almost instantaneously with the focusing of electron beam for the observation with a brighter contrast. They are not inherent to the implanted Al originally, but are attributable to the electron beam focusing effect. The degree of the focusing was roughly 50nA on the specimen area of about 1μm diameter, giving the electron flux of about 4×10^{19} electrons/cm$^2\cdot$s. Before the focusing, when looking for the area to be observed with less focused beam, we can never observe the appearance of such speckled areas. Further, these speckled areas can never be observable in hydrogen implanted Al under exactly the same experimental conditions with the deuteron implanted case. (So far we have done several ten times of the hydrogen implantation experiment.) This is readily seen in the micrograph (a) of Fig.2.

To observe the speckled area, there is a region of optimum fluence of deuteron ions, which produce the microstructure like those shown in Fig.2. For lower fluence than that of the optimum region, we observe only bubble structures and never observe the speckled area, and for higher fluence

than that, we observe, in addition to the T.S. structure, the bubble structure again and never observe the speckled area.

For crystallographic investigation of the speckled areas, selected area electron diffraction was tried on about 500nm area surrounding the speckled area. Those inserted in Fig.2 show the diffraction patterns taken on the areas seen in the micrographs. One should pay attention that (b-1) in Fig.2 (b), which was taken at the speckled area, clearly demonstrates the polycrystalline pattern with co-central spotty circular rings. On the other hand, the diffraction patterns from the normal areas, (a-1) and (b-2), show only usual Bragg spots showing single crystalline Al. So far we have observed five polycrystalline rings from several speckled areas of different specimens. The lattice constants corresponding to the rings are tabulated in Table 2, together with the lattice constants and corresponding planes inherent to Al.

To confirm the correspondence between the polycrystalline rings and the speckled area, dark field images were taken using several spots on the rings. Fig.3 (a) shows the bright field image of the speckled area with the diffraction rings, and (b) shows the dark field image of the same area taken with several diffraction spots on the rings. They show evidently that the polycrystalline spots originate from several parts of the speckled area, which appear brighter in (b).

The appearance of the speckled areas on the electron beam focusing is so rapid that we could not follow the detailed process, specially in its initial stage less than 10 seconds, of the appearance during the observation. However, after the appearance the images change rather

gradually as seen in Fig.4. In this figure, (a) was taken in roughly 10 seconds or so after the appearance, and (b) and (c) were taken sequentially in less than roughly 60 seconds after (a). In (a), images of the regions are very likely those of liquid state. These micrographs show rather gradual polycrystallization, judging from the growth of small crystallites as seen in (b) and (c), and the gradual change of equal thickness fringes as shown by an arrow. The change of the equal thickness fringes is presumed due to the thermal conditions around the region. The image did not change anymore after (c).

These observations indicate a rapid melting and gradual crystallization, which is rather conceivable if we assume that some kind of reactions in D_2 collections occurred suddenly and was maintained for a short time, evolving a large amount of heat during that time.

In addition to the above observations, we tried stereographic observations of the speckled region with change of the tilt angle of about 6 to 8 degrees to measure the depth of the layer in which the polycrystals are laying. As a result, we found that they are contained within the surface layer of the specimen having thickness of roughly 100nm above the T.S..

The duration of the reaction can be estimated from the extent of the melted region. Assume that the surface layer above the T.S., which is of about 90nm thick, has melted down during the time τ. From diffusion theory, the duration τ can be calculated as

$$\tau = \frac{W^2}{4D} = 2 \times 10^{-11} \quad \text{sec} \qquad (2)$$

where $D=0.78cm^2/s$ is the mean thermal diffusion constant of Al in the temperature region higher than room temperature and w=90nm is the surface layer thickness. The diffusion constant was obtained by use of the thermal conductivity $2W/cm \cdot K$, the specific heat $0.25cal/g \cdot K$ and the density $2.7g/cm^3$ of Al. In this calculation we assumed that the temperature rise at the bottom of the surface layer spreads towards the free surface. When assumed that the center of the speckled region is heated first and temperature spreads laterally, w should be 100nm or more, which give somewhat larger values for τ.

The experimental results described above clearly show that the speckled areas appeared on the electron bombardment are due to the local transformation from single crystalline to polycrystalline Al.

As far as the present authors are aware, the transformation from single crystalline to polycrystalline structure of Al metal with purity of 99.99% or above can never be achieved without melting and subsequent rapid solidification. One might inquire that the melting may induce evaporation of Al in high vacuum of electron microscope. However, the evaporation of Al on melting does not take place usually due to the firm protection of the melt surface by the oxide film even after the chemical etching.

Now we evaluate the amount of the heat evolution necessary for the observed local melting. We know already that the implanted deuterium molecules aggregate at the depth around 90nm from the surface when the deuterons were implanted perpendicularly from the surface. (The profiles shown in Fig.1 were taken under the implantation with 40° from the surface

normal.) From our observations so far undertaken, the extent of the transformed region occupies, on the average, $1 \times 10^{-9} cm^2$ of the surface. Taking the cover thickness of Al on the T.S. as 90nm, weight of Al contained in the polycrystalline transformation becomes $2.4 \times 10^{-14} g$. The heat necessary to raise the temperature of this amount of Al from 300K to melting point 933K is $q = 633 \times 0.25 \times 2.4 \times 10^{-14} = 3.8 \times 10^{-12}$ cal, where the specific heat of Al in this temperature range is 0.25 cal/g · K. The latent heat of melting of Al is 2.58×10^3 cal/mol [10], which gives the total latent heat for the melting of the above amount of Al $L = 2.58 \times 10^3 \times 2.4 \times 10^{-14}/27 = 2.3 \times 10^{-12}$ cal. Therefore, the whole heat necessary for the melting becomes, averaging on the several transformed regions, $Q = q + L = 6.1 \times 10^{-12}$ cal = 159 MeV for each transformed region.

Here, we would like to mention that the above estimation of the energy evolution could be smaller than that of whole energy evolved, since we have totally neglected the heat conduction though Al specimen. As mentioned before, the bottom side of the specimen below the T.S. is far thicker than the top side. So, a large amount of heat evolved in the D_2 collections in T.S. is presumed to flow out of the specimen though the thick bottom part to the specimen holder. Therefore, the heat responsible for the melting of the top area of the specimen must be a part of the whole heat evolution.

Now, we like to add the following experimental fact, that the melting was never observed when the specimens were kept at room temperature for rather long time after the deuteron implantation as shown in Fig.5, which was observed on keeping the specimen for about 24 hours at room

temperature after the deuteron implantation. The microstructure is very similar with those in which the melting was observed, for example that shown in Fig.2 (b). When the specimens were kept in liquid nitrogen, on the other hand, we could observe the melting even after more than 24 hours of the implantation.

5. Discussions and conclusion

One of the authors (K.K.) has published papers [1,2] describing the particle emission from implanted Al on the electron bombardment. The present experimental results have close similarities with this particle emission experiment in two aspects. First of all, it is requisite to focus the electron beam to observe both the polycrystalline transformation and the particle emission. Secondly, the optimum implantation fluence around $5\times 10^{17}D^{+}/cm^{2}$ is common in both experiments, which produces the T.S. with the smallest amount of coexisting bubbles. Neither lower nor higher fluence does produce the heat evolution and the particle emission as well. However, the difference of the two kinds of experiment is that in the present experiment we could never observe the heat evolution, to an extent which can melt even a part of Al, in hydrogen implanted case, and, on the other hand, in the particle emission experiment, we observed the particle emission in both hydrogen and deuterium implanted cases. We speculate that though the reactions in deuterium are accompanied with the heat evolution, the reactions in hydrogens, on the other hand, could be such as not accompanying a much heat evolution like the deuteron case. The two reactions are not necessarily the same reactions at all.

In the following, we raise the two kinds of possibility which are usually considerable for the melting, but not acceptable, as evidenced below, in the present situation.

5.1) Thermal insulation

Since the subsurface layer, which is of about 100nm in thickness, may be thermally insulated locally by the deuterium contained T.S. from the bulk of the specimen, the energy dissipation of the impinging electrons might raise the temperature of the layer up to the melting point. However, as is common in TEM experiment, main body of the impinging electrons usually pass through the specimen, as evidenced by observing sharp images of microstructures. Furthermore, we can raise an experimental evidence against such a suspicion.

As described at the end of the previous section, the melting does not occur when the implanted specimens are kept at room temperature for long time. On the other hand, the molecular density of deuterium decreases steadily with time at room temperature after the implantation as shown in Table 1. It means that the thermal conductivity of the deuterium collection in T.S. decreases steadily with time after the implantation. (The decrease of the thermal conductivities of hydrogen and deuterium with decrease of density in the fluid region are tabulated in Souers' book [11]). Further, the decrease of heat transfer coefficient between the Al and the fluid deuterium with the decrease of the latter density would enhance the thermal insulation. So, if the melting occurs because of the insulating effect of T.S., it must be observed more easily after keeping

the specimen at room temperature. It contradicts with the observation. Additionally, we presume that if the insulating mechanism works, the melting must be observed even in hydrogen implanted case, and further, the speckled region should not appear only in a limited region on a T.S., as observed in Fig.2 (b) and 4, but should occur on all over the T.S. region. The partial melting is presumably a result of a stop of the reaction in the fluid because of the decrease of deuterium density due to the escape out of the T.S. on the temperature rise of the specimen. In fact, the hydrogen profile like those of Fig.1 disappears on raising the specimen temperature up to 100℃ after room temperature implantation [5].

5.2) Decrease of melting point

Another point which we must be aware of is the size effect of the melting point of metals. Melting point of a fine particle decreases with decrease of the particle size. However, according to both theoretical calculation on Al and experimental results on Pb [12], the decrease is negligible for particles with more than several 10nm in radius. In the present experiment. Al specimens were made in wedge shape by chemical etching using TENUPOLE to perform the TEM observations. With these specimens, the speckled regions are observable in a rather thicker part more than several 100nm. In a thinner part of the specimen, on the other hand, we could not observe any change of the image even on the electron beam focusing. It is because, we presume, in the thinner part of the specimen, which is less than about 100nm thick, implanted deuteriums are

easily escapable through free surfaces. It means that the size effect of the melting dose not play any role in the present experiment.

The third possible heating mechanism is that deuterons and/or deuterium atoms contained in T.S. acquire some kinetic energy and induce the local temperature rise on colliding against the T.S. cover.

5.3) Collision of energetic particles onto the wall of T.S.

We assume that some kind of reactions, irrespective of chemical or nuclear nature, takes place in the deuterium collections, and consequently the freed deuterons and/or deuterium atoms created by this reaction acquire a mean kinetic energy E_o.

As calculated in the Appendix, the energy deposition per unit area of the bottom of the melted region can be given by

$$\frac{E}{\triangle x \cdot \triangle y} = \frac{\bar{E}_o}{16} \cdot n_d \cdot \ell_m \cdot (1 - R_E)$$

$$= 16 \cdot \frac{n_d}{\left| \frac{dE}{d\ell} \right|} \cdot \left(\frac{\bar{E}_o}{16} \right)^2 \cdot \left[1 - R_E \left(\frac{\bar{E}_o}{16} \right) \right]$$

$$= 2.4 \times 10^{10} \cdot \left(\frac{\bar{E}_o}{16} \right)^2 \cdot \left[1 - R_E \left(\frac{\bar{E}_o}{16} \right) \right] \cdot \mathrm{MeV/cm^2} \qquad (3)$$

where $n_d = 1 \times 10^{22} \mathrm{cm^{-3}}$ and $\left| \frac{dE}{d\ell} \right| = 1.38$ eV/nm were used, and E_o is in eV. In eq.(3), the bottom area was seen the same with $\triangle x \cdot \triangle y$. In Fig.6, eq.(3) is plotted against E_o with and without taking into account of the energy reflection coefficient R_E, which was taken from [13]. Taking $\triangle x \cdot \triangle y = 10^{-9} \mathrm{cm^2}$ and E=160 MeV, we obtain in Fig.6

$$\overline{E_o} = 90 \text{ eV}$$

on taking into account of the energy reflenction, and

$$\overline{E_o} = 58 \text{ eV}$$

on neglecting the energy reflection.

These results clearly show that any kind of chemical reactions can not be assigned to the cause of the melting observed, since chemical reactions can never produce such high kinetic energies whatsoever.

In connection with the above energy deposition, one may assume that deuteron produced by secondary electron bombardment is able to release 13.6eV each when they collide with the Al wall on recombining with a free electron thereupon.

Utilizing the calculation described in the Appendix, the total energy release on the de-ionization can be calculated as follows; i.e. the total energy relase E_R is the product between the amount of energy release, namely the ionization energy u_o, per impinging particle and the number of the impinging particles. Therfore, the total energy release becomes

$$E_R = u_o \int_{\triangle x} \int_{\triangle y} \int_0^{\ell_m} \int_{\omega} n_d \cdot dz dy dz \quad \frac{d\omega}{4\pi}$$

$$= u_o n_d \triangle x \triangle y \int_0^{\ell_m} dz \int_{\ell_m - Z}^{\ell_m} \frac{1}{2} \frac{(\ell_m - Z)^3}{\ell^4} \, d\ell$$

$$= \frac{1}{8} \quad u_o \cdot n_d \cdot \triangle x \cdot \triangle y \cdot \ell_m$$

$$= \frac{1}{8} \quad u_o \cdot n_d \cdot \triangle x \cdot \triangle y \cdot \quad \frac{\bar{E}_o}{\left| \frac{dE}{d\ell} \right|}$$

Calculating the necessary $\overline{E_o}$ to give the total energy release E_R=160 MeV, we have

$$\overline{E_o} = \frac{\left| \frac{dE}{d\varrho} \right|}{u_o \cdot n_d \cdot \triangle x \cdot \triangle y} E_R$$

$$= 64\,eV$$

which is much higher kinetic energy to reconcile the melting with the chemical reaction as mentioned before.

Altogether, we can conclude that any kind of chemical reactions can not be the cause of the melting observed in the T.S. cover. Since the heating effect of the energetic electron beam can not be also the cause of the melting as described before, the conclusion is inevitable that some kind of nuclear reactions is responsible for the melting.

When we assume, though tentatively, that 3 MeV p^+, or 0.8MeV α particles are emitted as a result of d-d nuclear reaction, the melting can be explainable rather easily. The stopping powers of 3 MeV p^+ and 0.8MeV α in Al are 21keV/μm and 340keV/μm, respectively. It means that the energy losses δE through 100nm Al are respectively 2.1keV and 34keV for the p^+ and α. Then, the necessary numbers of particles to give the energy deposition of 160 MeV, namely 160 MeV/δE, become 2×10^5 and 1×10^4 for p^+ and α, respectively, provided all particles get through the specimen in a short time like that calculated in eq. (2). Since the number of D_2 molecules contained in T.S. under the melted region is roughly 10^8, the above number of particles, which can be seen as the number of reacting d-d pairs, is a small fraction of the number of molecules, even if

we took into account of the solid angle in emitting the particles from the D_2 collections.

Lastly, we like to emphasize that, from the ERD and TEM investigations, we could not detect any remarkable differences in both density and depth distribution between the implanted hydrogen and deuterium in Al within the experimental errors. So we can not ascribe the observed difference between deuterium and hydrogen implantation cases, namely the melting and not-melting, to the molecular distributions.

As a conclusion, we can not explain the observed melting by any kind of chemical reactions. We presume that some kind of nuclear reactions are responsible for the melting.

Acknowledgement

Financial supports by the Tokyo Club and Light Metal Educational Foundation are greatefully acknowledged. The ERD studies described above were done under the collaboration with Prof. S. Yamaguchi of the Research Institute for Iron, Steel and Other metals of Tohoku University. The author (K.K) express his thanks for the collaboration.

Appendix

Energy deposition on the subsurface layer

In the following, we calculate the energy deposition of a particle reaching on a plane after suffering energy dissipation due to the collisions with surrounding particles.

This calculation aims at to obtain the mean kinetic energy of a deuteron contained in T.S., which is capable of depositing energy necessary to melt the T.S. cover, typically 160MeV. In this calculation we have to take into account of the energy dissipation of the moving particles due to the interaction between particles, because of the high density, i.e. 10^{22}molecules cm^{-3}, of the deuterium collection. According to the collision theory in solid [14], the energy of a moving deuteron E_{ex} necessary for the electron excitation in d-d collisions is more than 12.5keV, which is much higher than that expected in the present situation. Therefore, we assume that the deuterons suffer the stopping power due to the elastic collisions which is almost constant in the energy range less than E_{ex}.

For this calculation, we set a coordinate system as shown in Fig. A-1. A particle starting at z along the θ direction with an initial kinetic energy E_o hits the plan S, namely the bottom of the surface cover of T.S., with the kinetic energy

$$\bar{E}_o - \left| \frac{dE}{d\ell} \right| \cdot \ell$$

The stopping power is written as $-\left(\frac{dE}{d\ell} \right)$, and ℓ is the distance between the starting point z and the final point on the plane. Assuming a randum motion of the particle, the energy deposited is given by

$$\delta E(z) = \left(\bar{E}_o - \left| \frac{dE}{d\ell} \right| \ell \right) \cdot \frac{d\omega}{4\pi}$$

$$= \left(\bar{E}_o - \left| \frac{dE}{d\ell} \right| \ell \right) \frac{1}{2} \sin\theta \cos^2\theta \, d\theta$$

$$= \frac{1}{2} \bar{E}_o (\ell_m - z)^3 \cdot \frac{(1 - \beta\ell)}{\ell^4} \, d\ell$$

where $d\omega = dS \cdot \cos\theta / \ell^2 = 2\pi \sin\theta \cos^2\theta \, d\theta$ is the solid angle extended by the circular ring dS between $\theta \sim \theta + d\theta$ against the point z, and we used the relation $\ell\cos\theta = \ell_m - Z$ to

change the variable from θ to ℓ with Z fixed. β is given by

$$\beta = \frac{1}{\bar{E}_o} \left| \frac{dE}{d\ell} \right| .$$

ℓ_m is the length which satisfies $\bar{E}_o = \left| \frac{dE}{d\ell} \right| \ell_m$, namely $\beta \ell_m = 1$,

and is a function of $\bar{E}_o$.

Performing the integration on ℓ with z fixed,

$$\begin{aligned}
\triangle E(z) &= \int \delta E(z) \\
&= \int_{\ell_m - z}^{\ell_m} \frac{1}{2} \bar{E}_o (\ell_m - z)^3 \frac{(1 - \beta\ell)}{\ell^4} \, d\ell \\
&= \frac{1}{2} \bar{E}_o \left[\frac{1}{\ell_m^2} \left(-\frac{1}{3\ell_m} + \frac{\beta}{2} \right) (\ell_m - z)^3 - \frac{\beta}{2} (\ell_m - z) + \frac{1}{3} \right]
\end{aligned}$$

The total energy deposition is then given by integrating over all particles, i.e.

$$\begin{aligned}
E &= n_d \int_{\triangle x} dx \int_{\triangle y} dy \int_0^{\ell_m} dz \int_{\triangle \omega} [E_o - \qquad \ell] \qquad \cdot (1 - R_E) \\
&= \int_0^{\ell_m} \triangle E(z) \, dz \, n_d \triangle x \triangle y \cdot (1 - R_E) \\
&= \frac{\bar{E}_o}{16} n_d \triangle x \triangle y \, \ell_m \cdot (1 - R_E) . \qquad \text{(A-1)}
\end{aligned}$$

Where R_E represents the energy reflection coefficient [13]. Since $n_d \triangle x \triangle y \, \ell_m$ is the total number of particles which are able to contribute to the energy deposition, mean energy deposition

$\langle \varepsilon_o \rangle$ per impinging particle becomes

$$\langle \varepsilon_o \rangle = \frac{\bar{E}_o}{16} . \qquad \text{(A-2)}$$

Therefore, the energy reflection coefficient R_E must be read as a function of $\bar{E}_o/16$.

Reference

[1] K. Kamada ; Jpn. J. Appl. Phys. 31 (1992) L1289

[2] K. Kamada, M. Nakajima, M. Ogawa, T. Goto and H. Kakihana ; Proc. 7th Int. Conf. on Emerging Nuclear Energy Systems (ICENES '93, ed. H. Yasuda), P.168, Sept. 1993

[3] K. Kamada ; J. Nucl. Mater. 169 (1989) 141

[4] K. Kamada, A. Sagara, H. Kinoshita and H. Takahashi; Rad. Effects 103 (1987) 119

[5] K. Kamada : unpuhlished work.

[6] A. Michels, W. De Graaff and G.J. Wolkers ; Appl. Sci. Res. Sect. A12 (1963) 9

[7] R.L. Mills, D.H. Liebenberg and J.C. Branson ; J. Chem. Phys. 86 (1978) 2663

[8] R.L. Mills, D.H. Liebenberg, J.C. Branson and L.C. Schmidt ; ibid. 66 (1977) 3076

[9] H.H. Anderson and J.F. Ziegler ; The Stopping and Ranges of Ions in Matter, Vol3, (Pergamon Press, New York, 1977)

[10] from American Institute of Physics Handbook, 3rd edition, (McGraw Hill, New York, 1972.), Sec. 4.

[11] P.C. Souers ; Hydrogen Properties for Fusion Energy, (Univ. Calif. Press Berkley, 1986), Chap. 10

[12] for example, M. Hasegawa, K. Hoshino and M. Watabe; J. Phys. F: Metal Phys., 10 (1980) 619.

[13] G.M. McCracken and P.E. Stott; Nucl. Fusion 19 (1979) 889

[14] M. W. Thompson ; Defects and Radiation Damage in Metals. (Cambridge

Univ., Cambridge, 1969) Chap. 5.

Figure captions

Fig.1 Implanted hydrogen (a) and deuterium (b) profiles on the implantation with 25 keV H_2^+ and D_2^+ ions, respectively, into Al with 40 degrees from a surface normal. Both profiles were measured with ERD using 2MeV He^+ during the implantation. In (a), lower fluence profile is also shown. In (b), surface peak of hydrogen was also measured simultaneously, which is presumably due to the absorbed water molecules.

Fig.2 Transmission electron micrographs of hydrogen, (a), and deuterium, (b), implanted Al. An example of the polycrystallized area on the electron bombardment is shown by an arrow in (b). Selected area diffraction patterns taken on normal T.S. area, (a-1) and (b-2), and that taken on the polycrystallized area, (b-1), are inserted.

Fig.3 Bright field, (a), and dark field, (b), images taken on the polycrystallized area in a deuterium implanted Al. The dark field image was taken with several diffraction spots on the circular rings of the inserted selcted area diffraction pattern.

Fig.4 Sequential TEM micrographs of the same area of a derterium implanted Al, which were taken in less than 60 seconds after the appearance of the speckled area. (a) was taken in less than 10 second, then (b) and (c) were taken in less than 60 seconds sequentially after (a).

Fig.5 An example of the transmission electron micrograph of deuteron implanted Al to a fluence of about $5 \times 10^{17} D^+/cm^2$, which was taken on keeping the specimen for more than 24 hours at room temperature after the implantation.

Fig.6 Dependence of the energy deposition per unit area of the surface cover on the mean kinetic energy of deuterons. Energy reflection at the impinging surface is taken into account in A and not in B.

Fig.A-1 The coordinate system used to calculate the energy deposition.

Table 1 Changes of molecular density, molar volume and pressure of hydrogen/deuterium molecules with the time elapsed after the implantation.

Time after implantation	Molecular densities (cm^{-3})	Molar volume (cm^3/mol)	Pressure (MPa)
0	1×10^{22}	60	54.5
20 min	0.86×10^{22}	67	47.5
24 hours	0.63×10^{22}	95	30.5
48 hours	0.57×10^{22}	105	27.4

Table 2 Lattice constants of the polycrystalline aggregates determined by electron diffraction with the camera length L=570mm and the wavelength of electron $\lambda = 2.99 \times 10^{-3}$nm. Lattice constants and corresponding lattice planes of Al are shown together for reference purpose.

Ring	d_{obs}(A)	d_{obs}(A)	d_{obs}(A)	d_{obs}(A)	d_{obs}(A)(hkl)
1	2.4024	2.3976	2.3549	2.3385	2.338(111)
2	2.0366	2.0609	2.0287	-	2.024(200)
3	1.4570	1.4511	1.4505	-	1.431(220)
4	1.2473	1.2398	1.2213	-	1.221(331)
5	0.9266	-	-	-	0.9289(331)

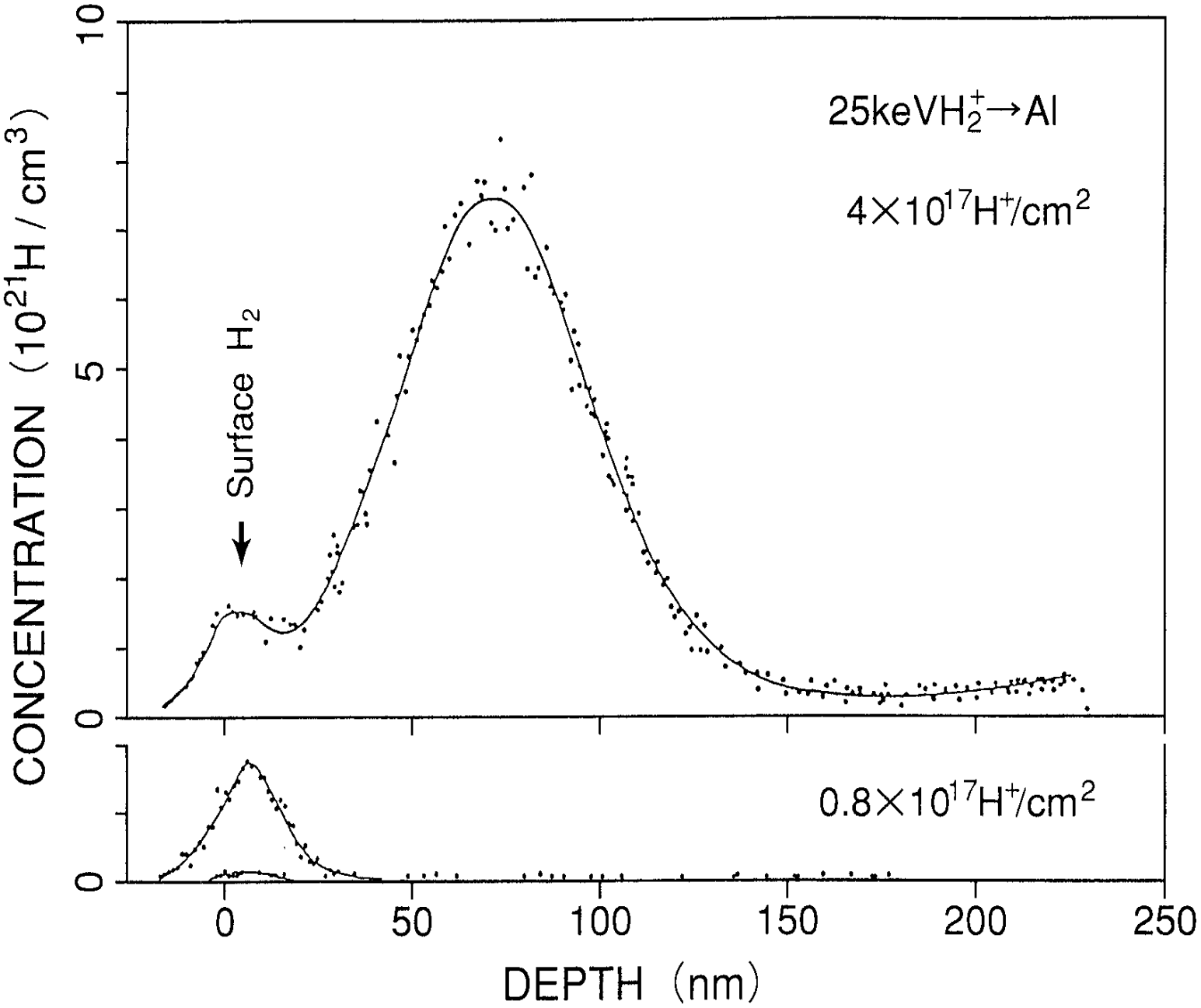
CONCENTRATION (10^21H / cm^3)
10
5
0
0
25keVH2+→Al
4×10^17H+/cm^2
Surface H2
0.8×10^17H+/cm^2
0
50
100
150
200
250
DEPTH (nm)

Fig. 1(a)

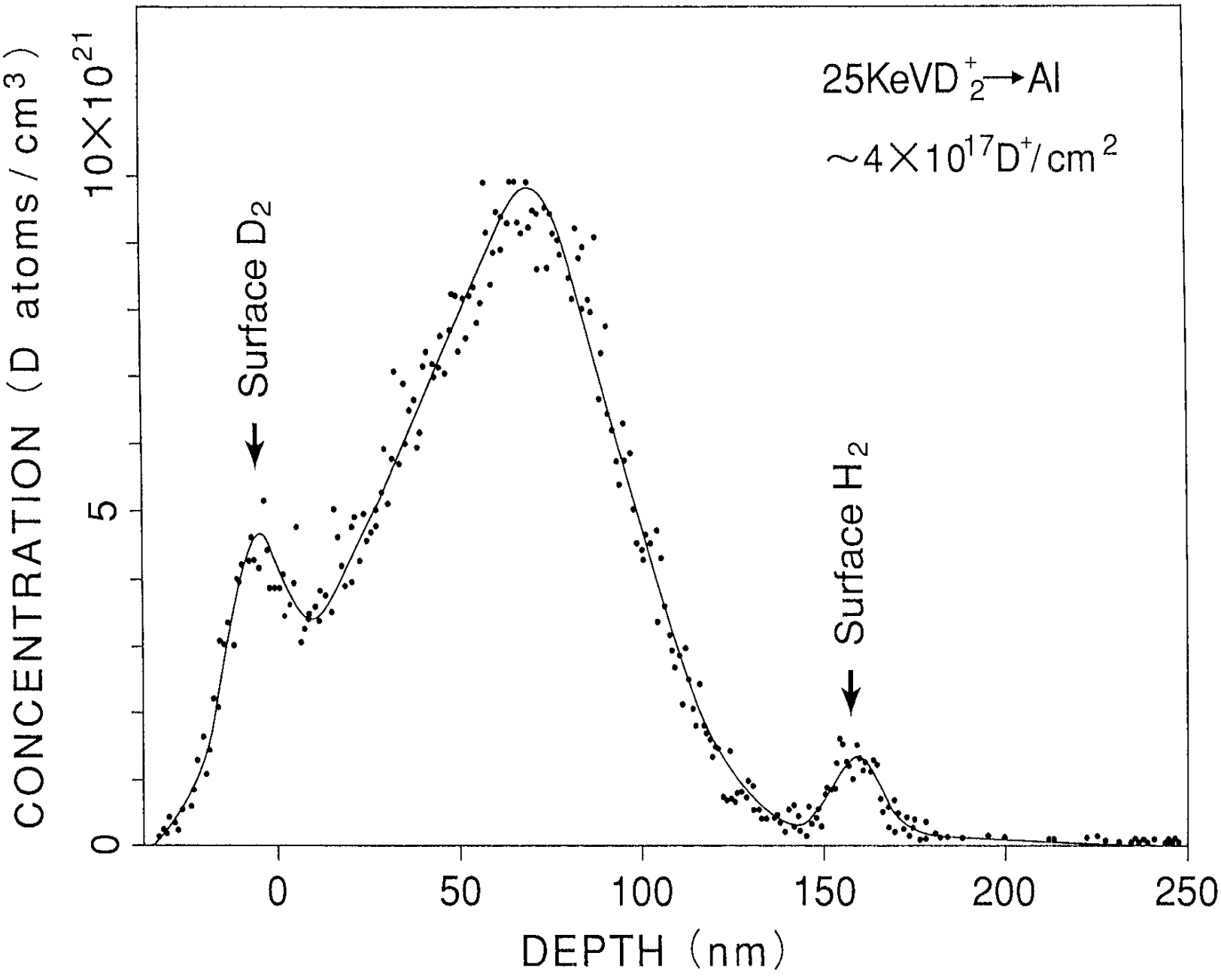
CONCENTRATION (D atoms/cm^3)
10X10^{21}
5
0
25KeVD$_2^+$→Al
~4X10^{17}D$^+$/cm^2
Surface D$_2$
Surface H$_2$
0
50
100
150
200
250
DEPTH (nm)

Fig. 1(b)

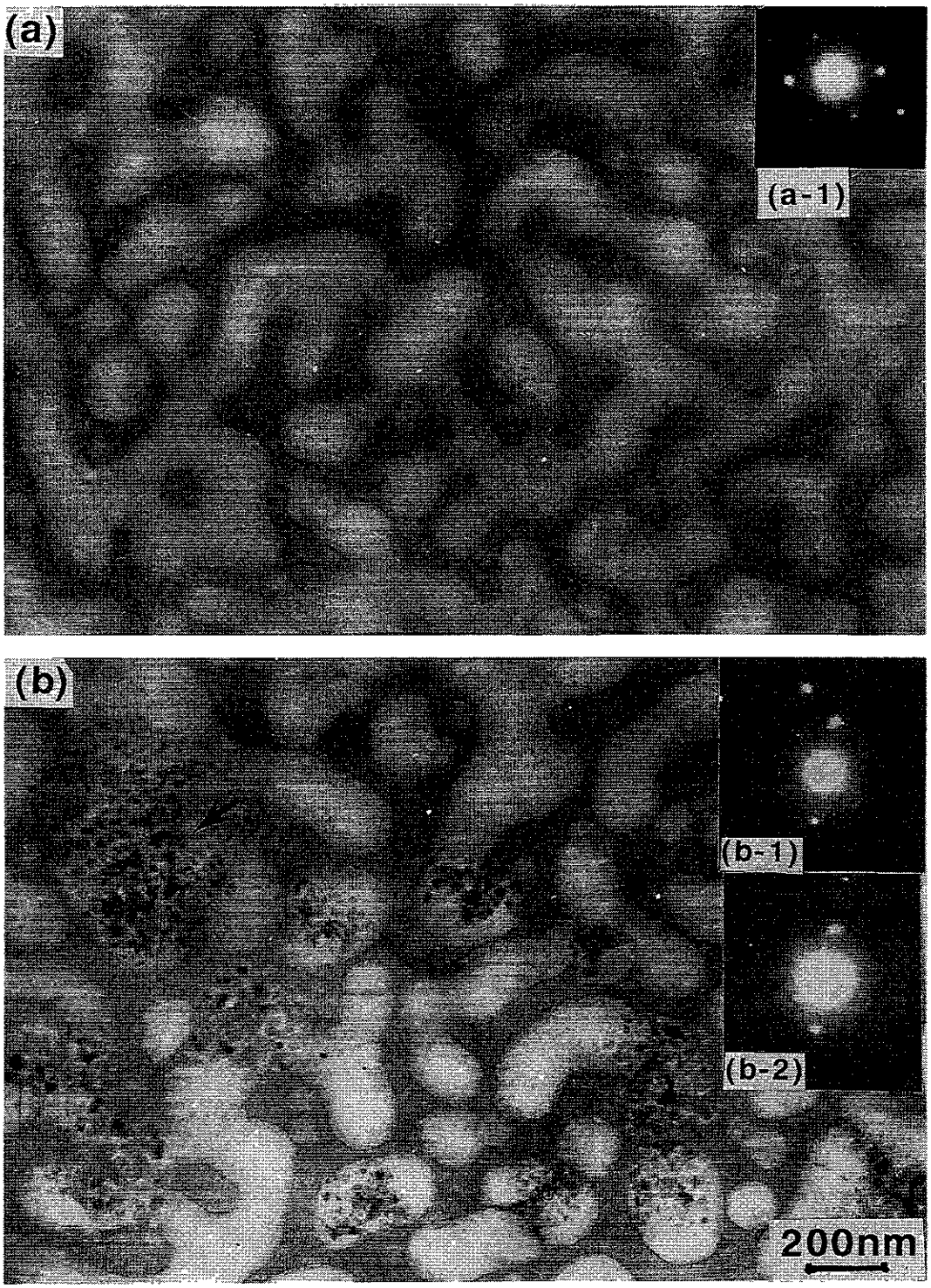

Fig. 2

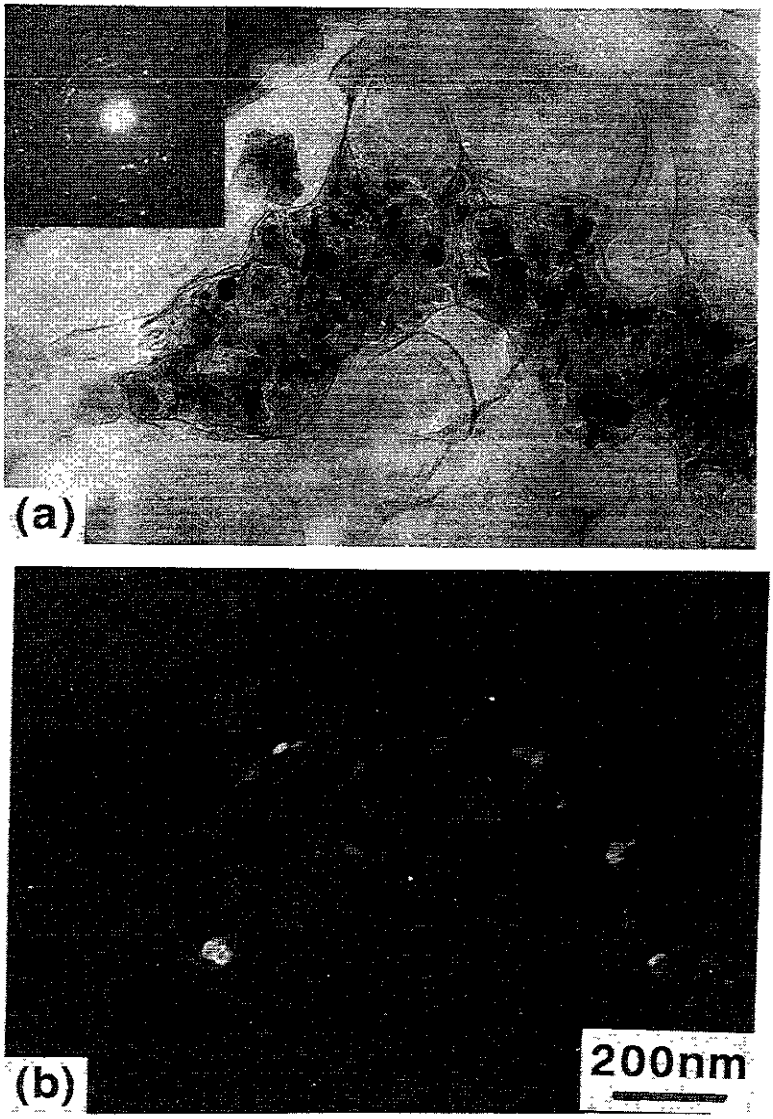

Fig.3

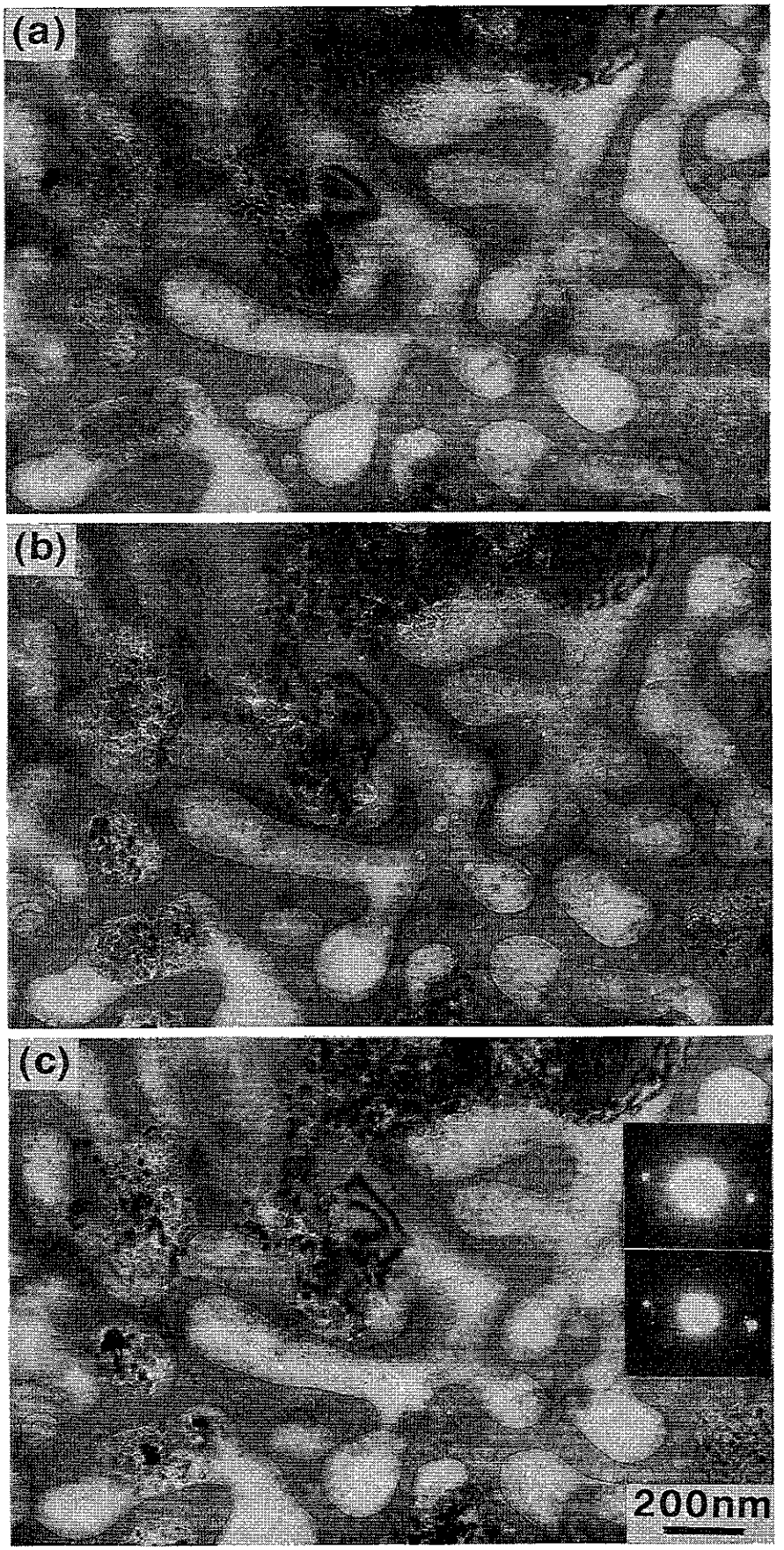

Fig. 4

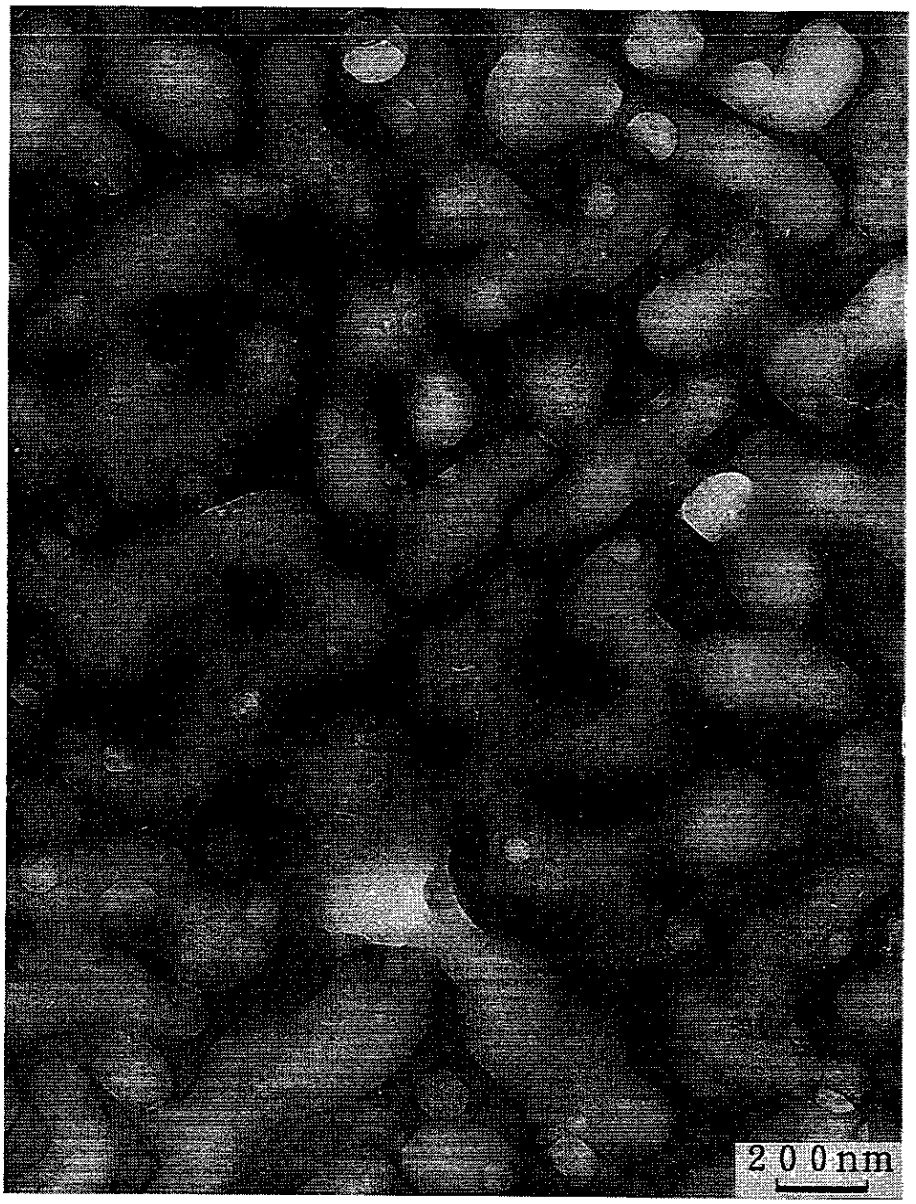

Fig. 5

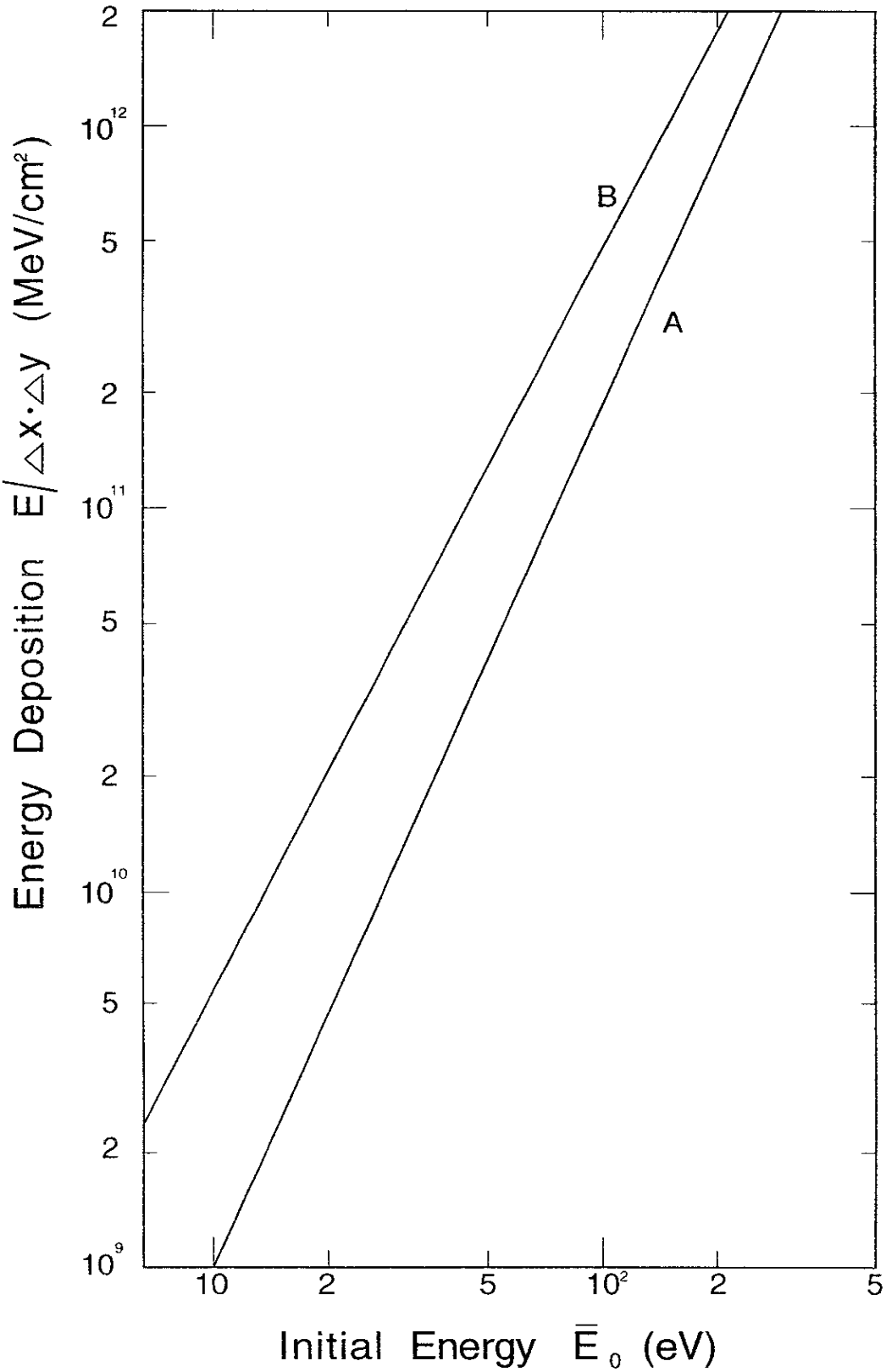
Energy Deposition E/△x·△y (MeV/cm²)
2
10¹²
5
2
10¹¹
5
2
10¹⁰
5
2
10⁹
B
A
10
2
5
10²
2
5
Initial Energy Ē₀ (eV)

Fig.6

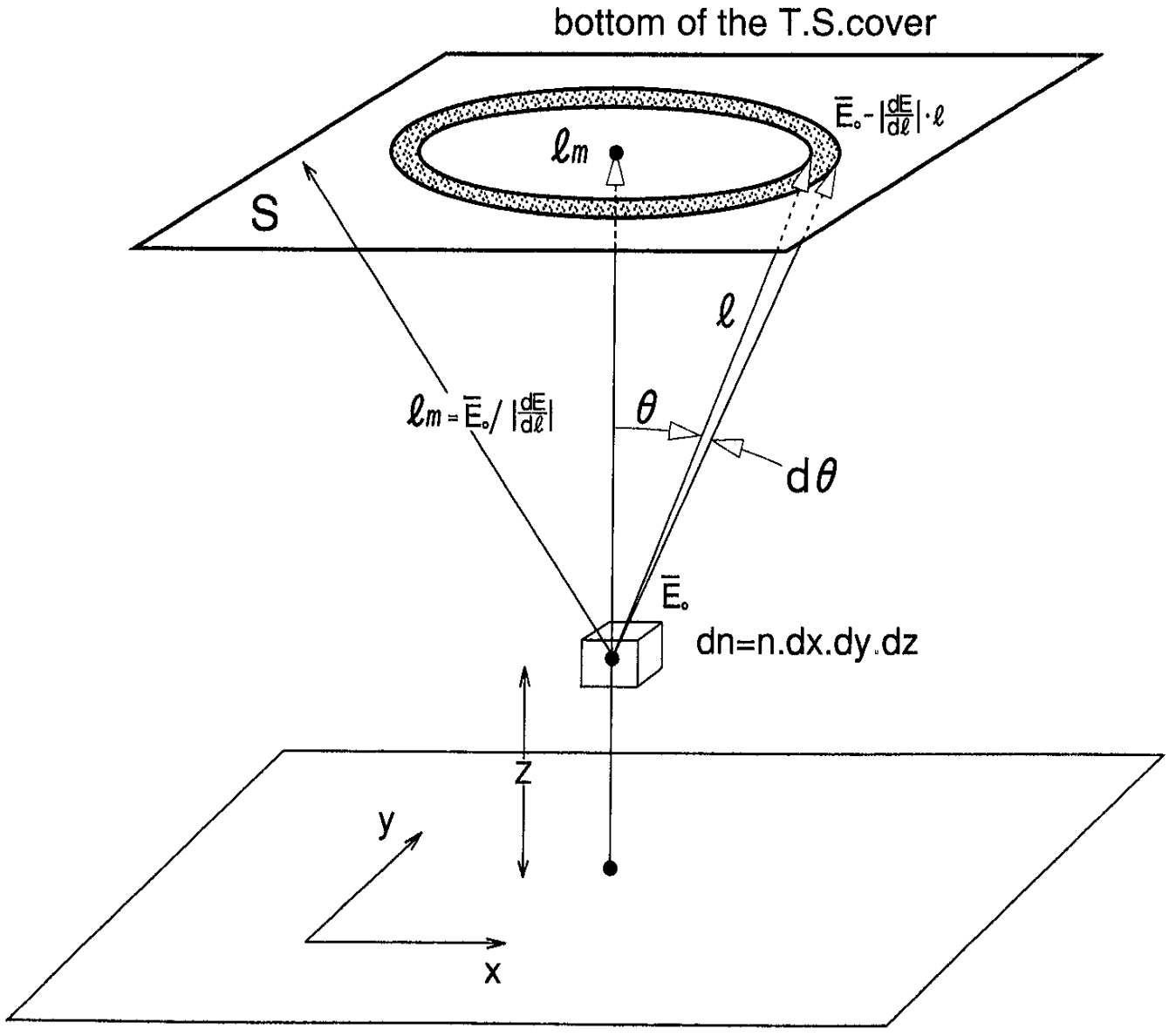
bottom of the T.S.cover
$\bar{E}_o - |\frac{dE}{d\ell}| \cdot \ell$
ℓ_m
S
ℓ
$\ell_m = \bar{E}_o / |\frac{dE}{d\ell}|$
θ
$d\theta$
$\bar{E}_o$
dn=n.dx.dy.dz
Z
y
x

Fig. A-1

Recent Issues of NIFS Series

NIFS-312 M. Salimullah, B. Dasgupta, K. Watanabe and T. Sato,
Modification and Damping of Alfvén Waves in a Magnetized Dusty Plasma; Oct. 1994

NIFS-313 K. Ida, Y. Miura, S -I. Itoh, J.V. Hofmann, A. Fukuyama, S. Hidekuma, H. Sanuki, H. Idei, H. Yamada, H. Iguchi, K. Itoh,
Physical Mechanism Determining the Radial Electric Field and its Radial Structure in a Toroidal Plasma; Oct. 1994

NIFS-314 Shao-ping Zhu, R. Horiuchi, T. Sato and The Complexity Simulation Group,
Non-Taylor Magnetohydrodynamic Self-Organization; Oct. 1994

NIFS-315 M. Tanaka,
Collisionless Magnetic Reconnection Associated with Coalescence of Flux Bundles; Nov. 1994

NIFS-316 M. Tanaka,
Macro-EM Particle Simulation Method and A Study of Collisionless Magnetic Reconnection; Nov. 1994

NIFS-317 A. Fujisawa, H. Iguchi, M. Sasao and Y. Hamada,
Second Order Focusing Property of 210° Cylindrical Energy Analyzer; Nov. 1994

NIFS-318 T. Sato and Complexity Simulation Group,
Complexity in Plasma - A Grand View of Self- Organization; Nov. 1994

NIFS-319 Y. Todo, T. Sato, K. Watanabe, T.H. Watanabe and R. Horiuchi,
MHD-Vlasov Simulation of the Toroidal Alfvén Eigenmode; Nov. 1994

NIFS-320 A. Kageyama, T. Sato and The Complexity Simulation Group,
Computer Simulation of a Magnetohydrodynamic Dynamo II: Nov. 1994

NIFS-321 A. Bhattacharjee, T. Hayashi, C.C.Hegna, N. Nakajima and T. Sato,
Theory of Pressure-induced Islands and Self-healing in Three-dimensional Toroidal Magnetohydrodynamic Equilibria; Nov. 1994

NIFS-322 A. Iiyoshi, K. Yamazaki and the LHD Group,
Recent Studies of the Large Helical Device; Nov. 1994

NIFS-323 A. Iiyoshi and K. Yamazaki,
The Next Large Helical Devices; Nov. 1994

NIFS-324 V.D. Pustovitov
Quasisymmetry Equations for Conventional Stellarators; Nov. 1994

NIFS-325 A. Taniike, M. Sasao, Y. Hamada, J. Fujita, M. Wada,

The Energy Broadening Resulting from Electron Stripping Process of a Low Energy Au^- Beam; Dec. 1994

NIFS-326 I. Viniar and S. Sudo,
New Pellet Production and Acceleration Technologies for High Speed Pellet Injection System "HIPEL" in Large Helical Device; Dec. 1994

NIFS-327 Y. Hamada, A. Nishizawa, Y. Kawasumi, K. Kawahata, K. Itoh, A. Ejiri, K. Toi, K. Narihara, K. Sato, T. Seki, H. Iguchi, A. Fujisawa, K. Adachi, S. Hidekuma, S. Hirokura, K. Ida, M. Kojima, J. Koong, R. Kumazawa, H. Kuramoto, R. Liang, T. Minami, H. Sakakita, M. Sasao, K.N. Sato, T. Tsuzuki, J. Xu, I. Yamada, T. Watari,
Fast Potential Change in Sawteeth in JIPP T-IIU Tokamak Plasmas; Dec. 1994

NIFS-328 V.D. Pustovitov,
Effect of Satellite Helical Harmonics on the Stellarator Configuration; Dec. 1994

NIFS-329 K. Itoh, S-I. Itoh and A. Fukuyama,
A Model of Sawtooth Based on the Transport Catastrophe; Dec. 1994

NIFS-330 K. Nagasaki, A. Ejiri,
Launching Conditions for Electron Cyclotron Heating in a Sheared Magnetic Field; Jan. 1995

NIFS-331 T.H. Watanabe, Y. Todo, R. Horiuchi, K. Watanabe, T. Sato,
An Advanced Electrostatic Particle Simulation Algorithm for Implicit Time Integration; Jan. 1995

NIFS-332 N. Bekki and T. Karakisawa,
Bifurcations from Periodic Solution in a Simplified Model of Two-dimensional Magnetoconvection; Jan. 1995

NIFS-333 K. Itoh, S.-I. Itoh, M. Yagi, A. Fukuyama,
Theory of Anomalous Transport in Reverse Field Pinch; Jan. 1995

NIFS-334 K. Nagasaki, A. Isayama and A. Ejiri
Application of Grating Polarizer to 106.4GHz ECH System on Heliotron-E; Jan. 1995

NIFS-335 H. Takamaru, T. Sato, R. Horiuchi, K. Watanabe and Complexity Simulation Group,
A Self-Consistent Open Boundary Model for Particle Simulation in Plasmas; Feb. 1995

NIFS-336 B.B. Kadomtsev,
Quantum Telegragh : is it possible?; Feb. 1995

NIFS-337 B.B.Kadomtsev,
Ball Lightning as Self-Organization Phenomenon; Feb. 1995

NIFS-338 Y. Takeiri, A. Ando, O. Kaneko, Y. Oka, K. Tsumori, R. Akiyama, E. Asano, T. Kawamoto, M. Tanaka and T. Kuroda,
High-Energy Acceleration of an Intense Negative Ion Beam; Feb. 1995

NIFS-339 K. Toi, T. Morisaki, S. Sakakibara, S. Ohdachi, T.Minami, S. Morita, H. Yamada, K. Tanaka, K. Ida, S. Okamura, A. Ejiri, H. Iguchi, K. Nishimura, K. Matsuoka, A. Ando, J. Xu, I. Yamada, K. Narihara, R. Akiyama, H. Idei, S. Kubo, T. Ozaki, C. Takahashi, K. Tsumori,
H-Mode Study in CHS; Feb. 1995

NIFS-340 T. Okada and H. Tazawa,
Filamentation Instability in a Light Ion Beam-plasma System with External Magnetic Field; Feb. 1995

NIFS-341 T. Watanbe, G. Gnudi,
A New Algorithm for Differential-Algebraic Equations Based on HIDM; Feb. 13, 1995

NIFS-342 Y. Nejoh,
New Stationary Solutions of the Nonlinear Drift Wave Equation; Feb. 1995

NIFS-343 A. Ejiri, S. Sakakibara and K. Kawahata,
Signal Based Mixing Analysis for the Magnetohydrodynamic Mode Reconstruction from Homodyne Microwave Reflectometry; Mar.. 1995

NIFS-344 B.B.Kadomtsev, K. Itoh, S.-I. Itoh
Fast Change in Core Transport after L-H Transition; Mar. 1995

NIFS-345 W.X. Wang, M. Okamoto, N. Nakajima and S. Murakami,
An Accurate Nonlinear Monte Carlo Collision Operator; Mar. 1995

NIFS-346 S. Sasaki, S. Takamura, S. Masuzaki, S. Watanabe, T. Kato, K. Kadota,
Helium I Line Intensity Ratios in a Plasma for the Diagnostics of Fusion Edge Plasmas; Mar. 1995

NIFS-347 M. Osakabe,
Measurement of Neutron Energy on D-T Fusion Plasma Experiments; Apr. 1995

NIFS-348 M. Sita Janaki, M.R. Gupta and Brahmananda Dasgupta,
Adiabatic Electron Acceleration in a Cnoidal Wave; Apr. 1995

NIFS-349 J. Xu, K. Ida and J. Fujita,
A Note for Pitch Angle Measurement of Magnetic Field in a Toroidal Plasma Using Motional Stark Effect; Apr. 1995

NIFS-350 J. Uramoto,
Characteristics for Metal Plate Penetration of a Low Energy Negative Muonlike or Pionlike Particle Beam: Apr. 1995

NIFS-351 J. Uramoto,
An Estimation of Life Time for A Low Energy Negative Pionlike Particle Beam: Apr. 1995

NIFS-352 A. Taniike,
Energy Loss Mechanism of a Gold Ion Beam on a Tandem Acceleration System: May 1995

NIFS-353 A. Nishizawa, Y. Hamada, Y. Kawasumi and H. Iguchi,
Increase of Lifetime of Thallium Zeolite Ion Source for Single-Ended Accelerator: May 1995

NIFS-354 S. Murakami, N. Nakajima, S. Okamura and M. Okamoto,
Orbital Aspects of Reachable β Value in NBI Heated Heliotron/Torsatrons; May 1995

NIFS-355 H. Sugama and W. Horton,
Neoclassical and Anomalous Transport in Axisymmetric Toroidal Plasmas with Electrostatic Turbulence; May 1995

NIFS-356 N. Ohyabu
A New Boundary Control Scheme for Simultaneous Achievement of H-mode and Radiative Cooling (SHC Boundary); May 1995

NIFS-357 Y. Hamada, K.N. Sato, H. Sakakita, A. Nishizawa, Y. Kawasumi, R. Liang, K. Kawahata, A. Ejiri, K. Toi, K. Narihara, K. Sato, T. Seki, H. Iguchi, A. Fujisawa, K. Adachi, S. Hidekuma, S. Hirokura, K. Ida, M. Kojima, J. Koong, R. Kumazawa, H. Kuramoto, T. Minami,. M. Sasao, T. Tsuzuki, J.Xu, I. Yamada, and T. Watari,
Large Potential Change Induced by Pellet Injection in JIPP T-IIU Tokamak Plasmas; May 1995

NIFS-358 M. Ida and T. Yabe,
Implicit CIP (Cubic-Interpolated Propagation) Method in One Dimension; May 1995

NIFS-359 A. Kageyama, T. Sato and The Complexity Simulation Group,
Computer Has Solved A Historical Puzzle: Generation of Earth's Dipole Field; June 1995

NIFS-360 K. Itoh, S.-I. Itoh, M. Yagi and A. Fukuyama,
Dynamic Structure in Self-Sustained Turbulence; June 1995